Acta Materialia 289 (2025) 120887

Contents lists available at ScienceDirect

Acta Materialia

journal homepage: www.elsevier.com/locate/actamat

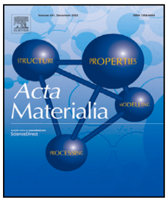

Full length article

Chemically ordered dislocation defect phases as a new strengthening pathway in Ni–Al alloys

H.C. Howard [a], W.S. Cunningham [a], A. Genc [a], B.E. Rhodes [a], B. Merle [b], T.J. Rupert [c,d], D.S. Gianola [a,*]

[a] Materials Department, University of California, Santa Barbara, Santa Barbara, 93106, CA, USA
[b] Institute of Materials Engineering, University of Kassel, Kassel, Germany
[c] Department of Materials Science and Engineering, Johns Hopkins University, Baltimore, 21218, MD, USA
[d] Hopkins Extreme Materials Institute, Johns Hopkins University, Baltimore, 21218, MD, USA

ARTICLE INFO

Keywords:
Dislocation
Defect phase
Complexion
Strengthening
Segregation engineering

ABSTRACT

There is emerging recognition that crystalline defects such as grain boundaries and dislocations can host structural and chemical environments of their own, which reside in local equilibrium with the bulk material. Targeting these defect phases as objects for materials design would promise new avenues to maximize property gains. Here, we provide experimental proof of a dislocation-templated defect phase using a processing strategy designed to engender defect phase transitions in a nickel-based alloy and demonstrate dramatic effects on strengthening. Following heat treatments designed to encourage solute segregation to dislocations, regions with introduced dislocation populations show evidence of nanoscale ordered domains with a $L1_2$ structure, whereas dislocation-free regions remain as a solid solution. Site-specific spherical nanoindentation in regions hosting dislocations and their associated ordered nanodomains exhibit a 40% increase in mean pop-in load compared to similar regions prior to the segregation heat treatment. Strength estimates based on random solute atmospheres around dislocations are not sufficient to predict our measured strengths. Our mechanical measurements, in tandem with detailed electron microscopy and diffraction of the ordered domains, as well as characterization of dislocations in the vicinity of the nanodomains, establish the defect phase framework via direct observations of chemical and structural ordering near dislocations and its potential for offering favorable properties not achievable through conventional materials design.

1. Introduction

Two central tenets have historically guided novel alloy design and its underlying fundamental science: (i) material properties are encoded through structural order, which can be controlled by processing, and (ii) defects in the otherwise perfect structure can be crucial in mediating performance-limiting properties. In the first viewpoint, bulk thermodynamics provides the road map for selecting the crystal structure and composition, while kinetic considerations guide the competition and possible suppression of phase evolution. The second principle builds on the first by acknowledging the often dominant role of defects, from atomic to microstructural scales, in mediating material properties and informing strategies for tailoring the spatial arrangement of defects [1–3]. The prevailing paradigm is to largely treat these considerations separately or sequentially, neglecting the impact of defects themselves on the chemical and structural ordering that underlies phase equilibrium in bulk materials [4]. However, recent evidence has demonstrated the existence of confined phases that emerge from, and remain anchored to, defects in crystals such as grain boundaries [5–7], planar faults [8–10], and dislocations [11–16]. These *defect phases* can exist in a local equilibrium with respect to the abutting phases and are not predicted by conventional bulk phase diagrams. Provided that the reduced dimensionality of the defect is appropriately considered [17], the adherence of defect phase equilibria to similar bulk thermodynamic and kinetic principles provides a pathway towards a “defects by design” framework that marries the two tenets above with the potential of achieving an unexplored property space. Accordingly, the principles for construction of defect phase diagrams have been reported [4,18–21].

Recent work has demonstrated the existence of confined phases at dislocations—the primary vehicle for plastic deformation—as evidenced by experimental measurements of compositional enrichment

---

* Corresponding author.

E-mail addresses: hhoward@ucsb.edu (H.C. Howard), streit@ucsb.edu (W.S. Cunningham), ardagenc@ucsb.edu (A. Genc), baileyrhodes@ucsb.edu (B.E. Rhodes), benoit.merle@uni-kassel.de (B. Merle), tim.rupert@jhu.edu (T.J. Rupert), gianola@ucsb.edu (D.S. Gianola).

https://doi.org/10.1016/j.actamat.2025.120887
Received 20 November 2024; Received in revised form 25 February 2025; Accepted 27 February 2025

and chemical ordering in the vicinity of dislocations and simulations showing localized disorder to order transitions [12,13,15]. The formation of dislocation phases is thought to be a consequence of the complex strain field surrounding the dislocation, which encourages local solute redistribution and drives structural and chemical transformation [4,11], notably under conditions where the bulk phase diagram would predict only a single phase. This phenomenon has been reported previously by Leyson et al. where they revealed the formation of defect phases surrounding dislocations due to an attractive H-H force experienced by hydrogen atoms as they are drawn closer together by dislocations [22]. Zhou et al. have reported Au segregation and defect phase formation at multiple types of defect structures including low-angle grain boundaries, stacking fault tetrahedra, Frank loops, and single dislocations in a Pt–Au alloy system [12]. Additionally, Kuzmina et al. and Da Silva et al. have shown the presence of dislocation phases in Fe-9 at.% Mn using atom probe tomography (APT) analyses of Mn segregation at dislocation cores, with the compositional enrichment of regions around dislocations suggesting a transition from α body centered cubit (BCC) to γ face centered cubic (FCC). The enriched FCC region does not coarsen even at very long annealing times (336 h), pointing to the confinement which distinguishes a dislocation phase from a process of heterogeneous nucleation that is predicted by the bulk phase diagram [13,14]. Using hybrid Monte Carlo and Molecular Dynamics (MC/MD) simulations, Turlo and Rupert identified dislocation phase formation in a dilute Ni–Al system where the increase in Al content at the dislocation encourages FCC to $L1_2$ transformation [15]. Singh et al. further evaluated Ni–Al for changes in stress–strain behavior and found increases in both break-away stress and peak stress for systems which contain dislocation phases compared to those that do not [23,24]. However, direct experimental observations of ordered phases confined to regions with large dislocation populations, as well as measurements of their impact on important engineering properties, have remained elusive.

Here, we aim to take advantage of the strengthening potential of defect phases by designing a processing route specifically targeting dislocation-mediated phase evolution within a model binary alloy system, Ni–Al, the primary building block for high performance superalloys used in extreme environments [25]. Our processing route consists of three basic steps: the generation of a super-saturated population of solute atoms serving as the reservoir for the defect phases, introduction of dislocations through a deformation process, and a secondary heat treatment designed to promote segregation of solutes to dislocations. We demonstrate direct evidence of nanoscale chemically ordered domains, causally linked to the presence of dislocations, through utilization of a suite of electron diffraction techniques and atomic-resolution electron microscopy, suggesting that the defects themselves template the local phases. Site-specific nanomechanical measurements of incipient plastic yielding demonstrate strengths associated with the presence of defect phases that far surpass both the baseline alloy values and those predicted for a random decoration of solutes around the dislocation cores, implicating the ordered dislocation phases as the origin of the ultrahigh strengths. Our results provide experimental proof of defect phases and demonstrate their potency in controlling material properties, paving the way for defect phases to be incorporated into more holistic materials design approaches.

2. Materials and methods

2.1. Sample preparation

Samples were generated via arc-melting to obtain a 20 g ingot of Ni-13 at.% Al, with compositions confirmed using Wavelength Dispersive X-ray Fluorescence (WDXRF) on a Rigaku ZSX Primus IV and via Energy Dispersive Spectroscopy (EDS) in the Thermo Scientific Apreo C LoVac Scanning Electron Microscope (SEM). The ingot was homogenized for 5 h at 1200 °C and quenched in water. Phase purity was evaluated using a Panalytical Empyrean Powder Diffractometer and analysis was performed using TOPAS Academic V7 [26], with additional confirmation from SEM.

Dislocations were introduced into samples in one of two ways (locally and globally) for subsequent testing. For the first set, samples were indented with a 1.6 mm radius spherical indenter with a Zwick 3212 Hardness Tester, and indent depth and size were measured using a Wyco NT1100 Optical Profiling System interferometer. This was done to locally introduce dislocations into the sample, generating regions of varying dislocation density within a single grain, as dislocation density decreases radially away from the indent. This was also done to ensure that all testing could be done on a single-crystal region to negate the effects of varied crystal orientation. In another set of samples, cold-rolling was used to reduce the sample thickness by 30%, introducing global distributions of dislocations. Some samples were then sealed in a quartz ampule under argon environment to undergo a second heat treatment, termed the "Defect Phase Heat Treatment" (DP-HT), which was performed for 3 h at 1050 °C to encourage solute diffusion towards the dislocations (Fig. 1).

2.2. Characterization and testing

On microindented samples, nanoindentation experiments were performed using a KLA iMicro Indentation System with a 1 μm diamond sphero-conical indenter tip where only the spherical apex makes contact with the sample. The effective radius is found to be consistent with the nominal radius of 1 μm, and a reduced modulus of 180 GPa is calculated based on the Young's modulus, E, and Poisson's ratios, ν of diamond (i, the indenter tip material) and Ni (m, the primary sample material) following the method of Oliver and Pharr [27]. Tests were performed at a strain rate of $10^{-3}\ \mathrm{s}^{-1}$ to generate a load–displacement curve with a maximum displacement of 50 nm (following the strain rate definition of [28]). At these shallow depths and with a small indenter tip, it is possible to probe highly localized dislocation phenomena. This testing was done in regions within the micro-indent (high dislocation density) and far from the micro-indent (low dislocation density) to compare behavior in these regions. Pop-in events were detected from the displacement signal by identifying time points at which the displacement rate jumped sharply. A threshold on the displacement rate of four times the root mean square error was used to ensure a jump in displacement was well outside the inherent noise of the signal. In this way, both the depth and load associated with the pop-in could be found.

Transmission electron microscopy (TEM) foils were pulled from different regions using a FEI Helios Dualbeam Nanolab 600 focused ion beam (FIB)-SEM. On rolled samples, TEM foils were prepared via electropolishing using a 10% perchloric acid and methanol mixture at −40 °C and with a 50 mA current in a Fischione Model 110 electropolisher. Samples were evaluated at 200 kV using collection angles of 9 mrad (bright field images) and 12–20 mrad (dark field images) on a Thermo Scientific Talos F200X TEM/STEM to confirm dislocation density in different regions and characterize the microstructure. Highly thinned regions of these samples were used for high-resolution STEM at 200 kV in a Thermo Scientific Spectra 200 TEM/STEM using a collection angle of 45–200 mrad. Where necessary, atomic-resolution STEM micrographs were processed using a custom non-rigid registration algorithm and filtered using a radial difference filter developed by HREM Research Inc. (high frequency maximum: 0.4, smooth edge: 0.2). To measure the size of ordered domains using the Fiji package of ImageJ [29], a bandpass filter which removes features larger than 50 pixels (14 nm) and smaller than 7 pixels (2 nm) in diameter was applied to the dark field TEM images. A linear contrast adjustment was also applied to improve the contrast between the background and bright ordered domains. Finally, the particles were analyzed without restricting the size or circularity. Cluster analysis was performed using a GPU-acceleration package for ImageJ, CLIJ2 [30]. Simulation of electron diffraction patterns was performed using JEMS and SingleCrystal software packages.

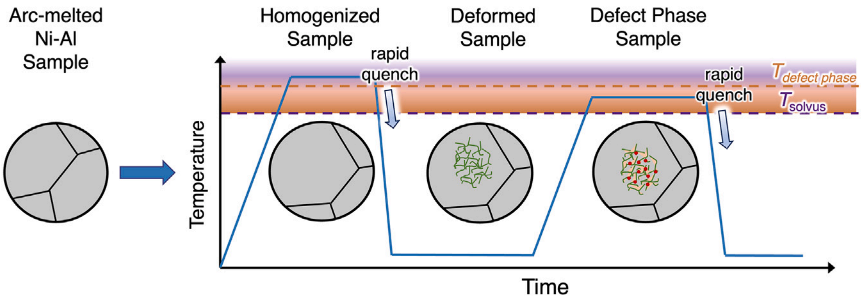

Fig. 1. Introduction of dislocations and specific heat treatment temperatures enable formation of defect phases. Process flow for sample preparation on a temperature vs. time plot. An arc-melted button of 13 at.% Al in Ni is homogenized at 1200 °C for 3 h. Microindentation or cold-rolling is then used to introduce dislocations within specific regions and grains in the sample. Finally, a second heat treatment is performed at 1050 °C to encourage solute diffusion to dislocations.

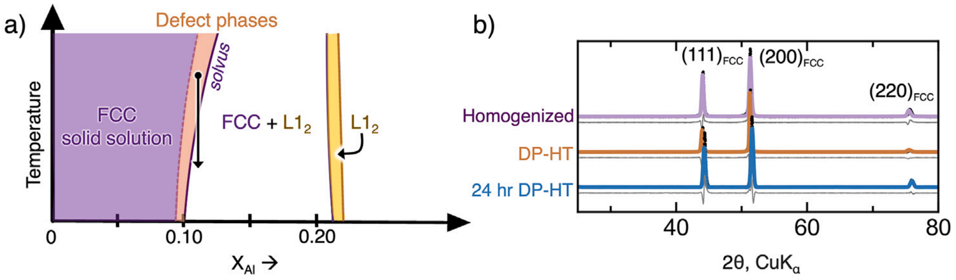

Fig. 2. Bulk characterization does not indicate bulk $L1_2$ formation. (**a**) Ni-rich side of the Ni–Al phase diagram showing the envelope in which dislocation phases can be expected to form. (**b**) Raw X-ray diffraction (XRD) data and the corresponding Pawley refinement fit for a sample after the homogenization heat treatment (purple), after the segregation heat treatment (orange), and after a long-term anneal (blue). XRD indicates only the presence of FCC Ni phase in all samples with no bulk formation of $L1_2$ (γ'). (For interpretation of the references to color in this figure legend, the reader is referred to the web version of this article.)

3. Results and discussion

3.1. Defect-aware processing strategy to generate dislocation defect phases

To demonstrate the versatility of our approach to various common processing methods, we employ two different modes of plastic deformation to introduce controlled populations of dislocations. In the first mode, we utilize spherical microindentation in a homogenized and water quenched super-saturated Ni-13 at.% Al alloy to generate a concentrated population of dislocations within a single crystalline grain. This allows for direct comparison between regions with varied dislocation densities within the same crystallographic orientation. Spherical indentation, unlike indentation with sharp tips, can span the elastic to plastic transition, providing careful control on both the amount of plastic strain and the dislocation density introduced [31,32]. The relative strain, ϵ_r, introduced by a round indenter is directly proportional to a/r during indentation, where a is the contact radius and r is the tip radius [33]. For samples shown in this work, the relative strain introduced is calculated to be ϵ_r = 3%–4% (supplementary text). Once dislocations have been introduced, a defect phase heat treatment (denoted “DP-HT”) is employed to enable solute diffusion to dislocations, driving localized defect phase formation. The temperature of this super-solvus heat treatment is chosen to lie within the single-phase face centered cubic (FCC) region, but near the solvus boundary (Fig. 2a) to be consistent with the predicted defect phase-forming envelope as described by Turlo and Rupert [15]. By choosing a temperature near the solvus, we improve the likelihood of forming dislocation phases, and by remaining outside of the two-phase region, we reduce the likelihood of nucleating bulk $L1_2$, either within the matrix or through a process of heterogeneous nucleation. As evidenced by laboratory X-ray diffraction (XRD), there is no indication of bulk phase evolution after either the homogenization heat treatment or the DP-HT following 1 h and 24 h of annealing (Fig. 2b).

To extend our approach to a bulk processing method, we use cold rolling (ϵ_p = 30–40%) as our second deformation mode to generate a higher, quasi-homogeneous dislocation distribution throughout the sample. In all samples, bulk microstructural characterization (XRD) indicates no phase change following the DP-HT; however, examination at finer length-scales from highly deformed regions suggests a more striking evolution, as evidenced by a marked difference in dislocation microstructure and diffraction signatures (Fig. 3). While samples prior to DP-HT contain a high dislocation density, there is no evidence of a secondary phase in real space images or diffraction (Fig. 3a,b). After the DP-HT (Fig. 3c) there are clearly distinguishable superlattice reflections (indicated by white arrows) visible in the selected area electron diffraction pattern (SAEDP) acquired from rolled samples, which can be directly indexed as $L1_2$ atomic ordering (Fig. S1). This is particularly obvious in intensity scans along the [002] direction, where peaks in intensity are observed at $g = [001]$ and $g = [00\bar{1}]$ (Fig. 3d).

A similar evaluation is performed on microindented samples in regions both within the indent and far away (“far field”), where the expected dislocation density is low. Similarly to rolled samples, dislocated regions before DP-HT do not show evidence of phase evolution either in real space (Fig. 4a) or diffraction (Fig. 4b). After DP-HT (Fig. 4c), we note a slight decrease in dislocation density from 3.9×10^{13} m^{-2} to 1.0×10^{13} m^{-2} and the emergence of intensity in the superlattice positions indicating $L1_2$. While these superlattice spots are more difficult to see in the raw diffraction pattern, intensity in the superlattice positions is made obvious in line scans along the [002] direction (Fig. 4d). The higher intensity of superlattice spots in rolled samples is consistent with the higher plastic strain and dislocation density present in that sample before DP-HT.

In the far field (Fig. 5a), BF-STEM imaging shows there are still some dislocations, although at a much lower density, and an SAEDP in this region does not show intensity in the superlattice positions (black line in Fig. 4d), indicating a lack of $L1_2$ formation. We therefore confirm that the superlattice reflections observed in both the microindented and cold-rolled samples following the DP-HT arise from the presence of localized $L1_2$ ordering and systematically rule out other sources of diffracted intensity, including Kikuchi line intersections, thermal and

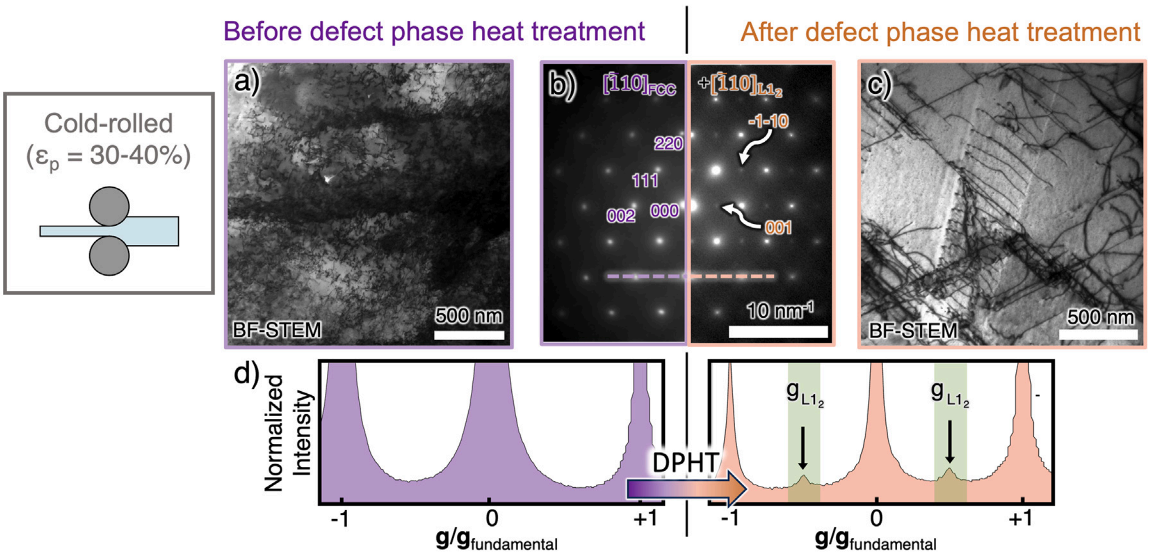

Fig. 3. Micrographs and diffraction patterns indicate phase evolution after DP-HT in rolled samples. (**a**) Bright field scanning transmission electron microscopy (BF-STEM) micrograph of a sample cold-rolled to 30% strain. (**b**) Selected area electron diffraction pattern (SAEDP) of a cold rolled sample before (left side) and after (right side) the DP-HT with superlattice spots indicated by arrows. (**c**) BF-STEM micrograph of a cold-rolled sample after DP-HT. (**d**) Intensity plots taken from line scans along the [002] direction for rolled samples, before and after DP-HT. Superlattice intensity is indicated with black arrows.

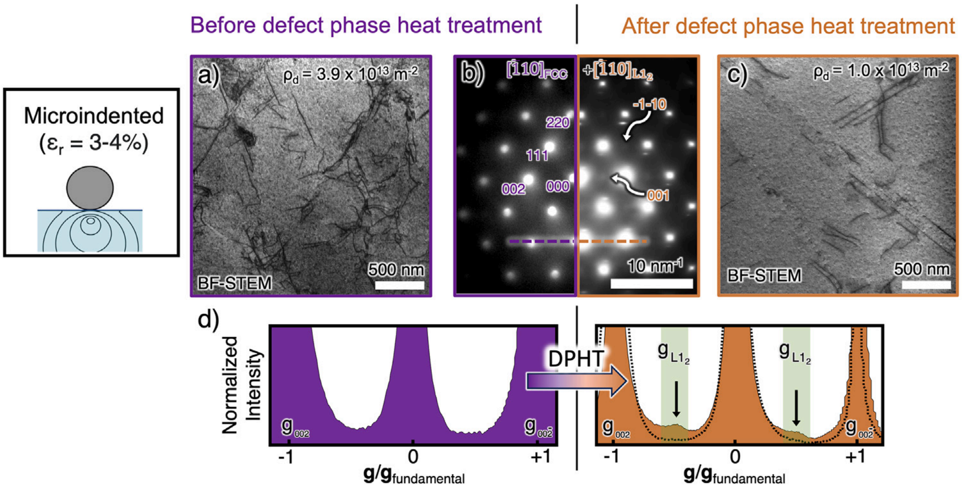

Fig. 4. Micrographs and diffraction patterns indicate phase evolution after DP-HT in microindented samples. (**a**) Bright field scanning transmission electron microscopy (BF-STEM) micrograph of a sample microindented to 3% relative strain. (**b**) Selected area electron diffraction pattern (SAEDP) of a microindented sample before (left side) and after (right side) the DP-HT with superlattice spots indicated by arrows. (**c**) BF-STEM micrograph of a microindented sample after DP-HT. (**d**) Intensity plots taken from line scans along the [002] direction for microindented samples, before and after DP-HT. Superlattice intensity is indicated with black arrows. The black dashed line shows a similar line scan in a region far from the microindent, indicating no phase evolution in this region.

static displacements, dynamical scattering and thin foil effects, and the presence of stacking faults (supplementary text, Figs. S2-S5) [34,35]. These differences in diffraction signatures before and after the DP-HT, and within heavily dislocated regions and in the far-field, causally link the presence of a dislocation population and local ordering, and suggest that the dislocations and their associated strain fields promote the transition from a disordered solid solution to a matrix containing ordered domains. We next ask whether the newly formed local dislocation environment following the DP-HT influences the mechanical behavior of the alloy using a site-specific technique to probe incipient plastic yielding, a deformation regime where dislocations would be expected to interact most strongly with obstacles generated in their direct vicinity.

3.2. Strength of alloy hosting dislocation defect phases

To evaluate the mechanical impact of dislocation defect phases in this Ni–Al system, Singh et al. have employed hybrid Monte Carlo/molecular dynamics simulations to directly compare dislocation glide in several key sample types [23]. When compared to a simple solid solution of Al in Ni (at concentrations ranging from 1 – 4 at % Al), the break-away stress for initial dislocation glide is increased by a factor of 4x, and the peak stress (analogous to a flow stress in their simulations) is increased by a factor of 1.3x for simulation cells containing dislocation defect phases. In addition, in contrast to the more traditional Orowan bowing mechanism, Singh et al. showed that the mechanism for unpinning from dislocation defect phases requires a characteristic bowing and “unzipping” motion [24]. This is caused by the presence of the dislocation phase domains slightly off the glide plane where they interact with the dislocation due to its hydrostatic stress field. These previous computational studies directly point to signatures of dislocation motion which we aim to probe experimentally with a specific emphasis on evaluating changes in incipient plasticity, or the exact moment of dislocation de-pinning.

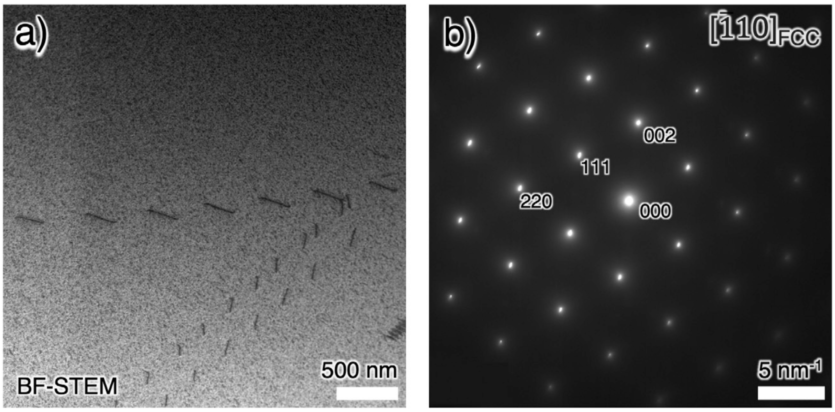

Fig. 5. Microscopy of regions with low dislocation density do not indicate any phase evolution. (**a**) Bright-field STEM image of a region far from the microindent (several hundred μm) where dislocation density is low. (**b**) SAEDP in this region, which shows no evidence of secondary phase formation (line scan is shown in Fig. 4d).

Nanoindentation "pop-in" testing can provide insights on dislocation-mediated mechanisms by probing highly localized regions of a sample [36–38]. The pop-in phenomena can be described as a rapid change in displacement at a constant load in a nanoindentation load–displacement curve which marks the transition from fully elastic deformation, where contact can be modeled using Hertzian contact theory, to elastic/plastic deformation [31]. More specifically, pop-in occurs when there is a sudden cascade of dislocation motion, either from dislocation nucleation or glide, and subsequently manifests as a sudden change in displacement. The explicit utilization of a spherical indenter tip allows for exploration of the elastic to plastic transition and observation of the onset of dislocation-mediated plastic deformation. However, the exact mechanisms governing pop-in can vary and depend on several parameters such as the indenter tip geometry and size, material microstructure, and defect environment under the indenter [38–41]. If there are very few dislocations in the material, it is highly unlikely that a dislocation will be present in the activation volume under the indenter tip, and therefore pop-in will occur due to dislocation nucleation near the theoretical strength [41]. When many dislocations are present, however, pop-in is more likely to occur at some stress value below the theoretical strength as dislocations are readily excited to glide [38]. As such, pop-in is dependent on the dislocation concentration of the material and any microstructure that may hinder or aid dislocation motion.

We employ spherical nanoindentation pop-in testing to evaluate incipient dislocation-mediated mechanisms in dislocated and heat treated samples by targeting specific regions of the microindented sample, as the pop-in load is correlated to the local dislocation content [36–38, 41]. We measure statistical distributions of pop-in loads obtained from load–displacement data during nanoindentation within and outside the microindent to reveal the influence of the ordered features arising from the DP-HT. Indeed, an initial examination of the load–displacement curves inside the microindent (Fig. 6b, c) indicates that the mean pop-in load is dramatically increased after the DP-HT from 87.3 μN to 253 μN. Away from the microindent, where dislocation densities are low (Fig. 6a), the distribution of pop-in loads is skewed towards high values, with a mean of 410 μN. This trend is a reflection of the low probability of activating existing dislocations under the indenter tip in a region where dislocations are sparse, promoting pop-in at higher loads where dislocation nucleation is required [38].

The dramatic drop off of the mean pop-in loads from the far-field to regions within the microindent also signals a mechanism change away from dislocation nucleation and towards activation (e.g. glide, de-pinning) of pre-existing dislocations [38]. Using these data, we calculate the maximum shear stress under the indenter tip at the pop-in load using:

$$\tau_{max} = 0.31\left(\frac{6}{\pi^3}\frac{PE_r^2}{R^2}\right)^{1/3} \tag{1}$$

where P is the load at pop-in, E_r is the reduced modulus, and R is the indenter tip radius [42]. Consistent with the qualitative observations from the load–displacement curves, the distribution of τ_{max} values from the far-field region (green circles in Fig. 7a) is consistently higher, with values approaching the theoretical strength of pure Ni [43] and displaying less scatter (Fig. 7a), again corroborating a nucleation-dominated regime. The broader tail at lower τ_{max} values likely reflects the low probability that a dislocation is encountered within the indented volume where lower stresses are required to activate glide. A best fit to these far field data using a stress-biased, thermally activated dislocation nucleation model (solid green line in Fig. 7a) yields activation volumes wholly consistent with homogeneous nucleation in FCC metals [44,45].

Specifically, these estimates for the dislocation nucleation regime are performed by modeling the cumulative distribution function of pop-in under an applied load as [44,45]:

$$f = 1 - exp\left[-\frac{\eta kT}{\dot{\tau} v^*} * exp\left(\frac{\tau v^*}{kT}\right)\right] \tag{2}$$

where η is the nucleation rate with no applied stress, k is the Boltzmann constant, T is temperature, $\dot{\tau}$ is loading rate, v^* is activation volume, and τ is the shear stress at pop-in. Using the fit to this model, the activation volume and energy can be calculated for the far-field data set, which are 22.7 Å^3 and 0.78 eV, respectively. These values are consistent with many other nanoindentation studies of incipient plasticity governed by dislocation nucleation in several materials [41,44,45]. Further insights on the magnitude of the activation volumes are aided by atomistic simulations, which indicate that dislocation loops do not necessarily nucleate at their equilibrium size under an indenter tip and instead grow from small regions of crystalline imperfections under the indenter tip [41]. Additionally, in a material which has been highly strained, dislocations are thought to potentially nucleate at vacancies or vacancy clusters [45,46], which may be present in excess amounts from either quenching or plastic deformation. Taken as a whole, we conclude that dislocation nucleation is necessary to observe pop-in in the far field.

3.2.1. Sources of strengthening in microindented regions

In the contrasting case where many pre-existing dislocations are present, the stress at which any dislocation may glide is more stochastic, as demonstrated by the broader τ_{max} distributions within the microindent (blue triangles and pink squares for before and after DP-HT, respectively), reflecting the activation of various dislocation environments which could be present under the indenter tip in this highly deformed region [40]. We note that, while high, these τ_{max} values inside the microindents are far below the theoretical strength measurements we would expect from dislocation nucleation, and the greater spread of the CDF curves indicates a more stochastic sampling of pre-existing dislocations [38,47]. The high τ_{max} values are also consistent

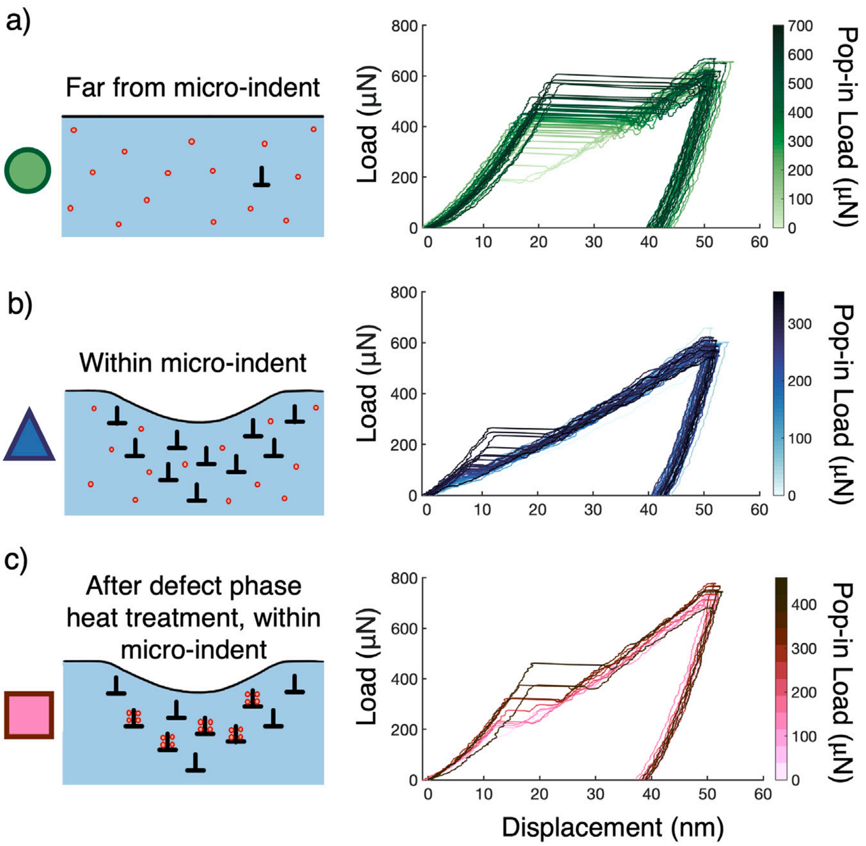

Fig. 6. Nanoindentation pop-in data indicates an increase in pop-in load after DP-HT. (**a**) Raw pop-in data from a region far from the microindent where few dislocations are expected. (**b**) Raw pop-in data from a region within the microindent, before the DP-HT, where there is a higher dislocation density. (**c**) Raw pop-in data from a region within the microindent after the DP-HT.

with what one might expect when probing plasticity in a very small volume [48–50] where source-controlled plasticity is dominant. Indeed, in the far field, we confirm this behavior and do not observe pop-in until nucleation occurs at very high stresses since there are few or no pre-existing dislocation sources available [40,41,51]. In contrast, in regions of higher dislocation density, a new relevant length scale apart from plastic zone size and indenter tip radius has been introduced, and we must consider how this impacts pop-in results. As summarized by Gao and Bei, pre-straining a material before very small-scale testing (including nanoindentation and micropillar compression) leads to lower max shear stresses but does not recover values that would be expected from bulk testing methods [47,52]. This is because, even when dislocations are present before nanoindentation, the small volume of the plastic zone will likely probe a highly limited number of dislocations which may not be ideally oriented for slip. Therefore, we expect all pop-in results, regardless of pre-existing dislocation density, to over predict the max shear stress of the bulk Ni–Al alloy, but the primary signature of interest is the difference between strength measured inside the microindent before and after DP-HT. Strikingly, the average normalized τ_{max} (assuming a shear modulus of μ = 74 GPa [53]) following DP-HT is well above the value from before DP-HT (Fig. 6E), increasing by about 40% from $0.031\mu \pm 0.0051\mu$ to $0.042\mu \pm 0.0053\mu$. We consider possible sources of strengthening that can explain this pronounced effect following the DP-HT where chemical ordering occurs in regions with high dislocation densities.

First, we consider strengthening owing to the presence of segregated solutes in proximity to dislocations that may be expected to create solute atmospheres. We apply the Labusch model [54,55] to predict the corresponding strengthening increment, $\Delta\tau_{\perp-solute}$, which accounts for the interaction forces between a dislocation and solute atoms (acting as pinning sites) assuming a non-dilute solute atmosphere both on and off the primary glide plane, and can be expressed as follows:

$$\Delta\tau_{\perp-solute} = 3\beta\mu\varepsilon^{4/3}c_{\perp}^{\alpha} \tag{3}$$

where μ is the shear modulus, ε is the misfit parameter, β is a fitting parameter dependent on the solvent, $c_{\perp}$ is the concentration of the solute atoms near the dislocation, and α ranges from 1/2 to 2/3 based on the strength of the pinning of the obstacle [55]. The misfit parameter, ε, encodes information on the modulus and size misfits of solute and solvent atoms and accounts for differences in interaction forces between screw and edge dislocations and solute atoms [56]. Mishima et al. experimentally estimated a collective value for these leading terms, termed the strengthening coefficient, $k = 3\beta\mu\varepsilon^{4/3}$, for Al in Ni by performing compression measurements on Ni–Al alloys ranging from 2 at.% - 8 at.% Al and measured the 0.2% flow stress as a function of concentration, yielding a direct measurement of k = 0.225 GPa [57]. More recently, Wang et al. employed density functional theory calculations to predict the relevant parameters for solid solution strengthening within the Labusch framework, namely the lattice mismatch and modulus mismatch due to solute atoms [58]. Based on their calculations and taking $\beta = 4.3 \times 10^{-4}$, $\mu = 74$ GPa, and $\varepsilon = 0.9$ when averaged for screw and edge dislocations, a value of k of 0.188 GPa is predicted, with the difference between this value and that of Mishima et al. likely arising from confounding strengthening effects in the experimental samples (e.g. grain boundaries, contaminants). For the sake of our analysis, we use both values to predict a range of possible strengthening from segregation of Al solutes to dislocations in our Ni–Al system. We further bracket the limits of this prediction by considering values of α between 1/2, when solute atoms are treated individually [59], to 2/3 when the solute is treated as a field which contributes a drag force to dislocation glide [54]. Using the range

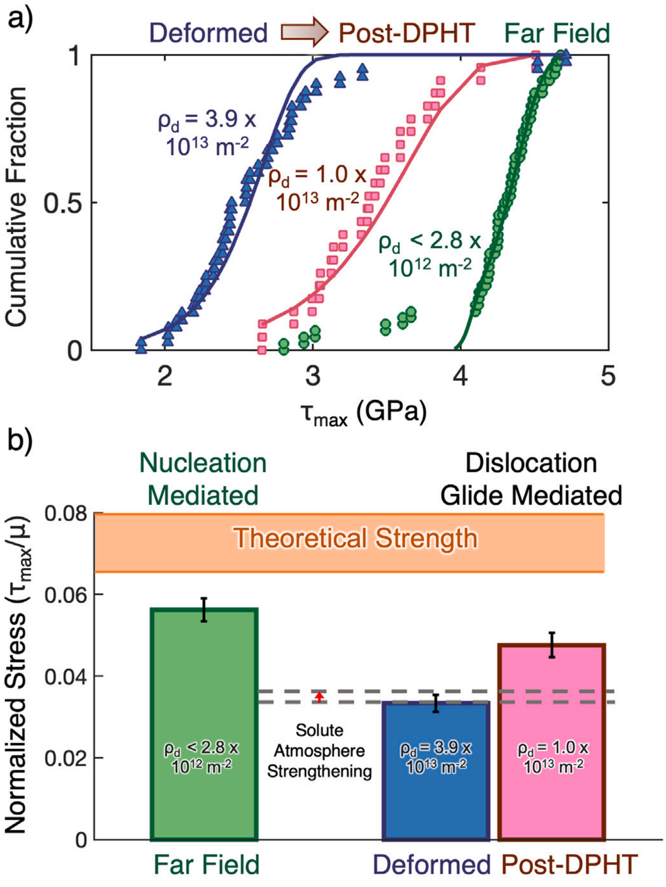

Fig. 7. Post DP-HT samples indicate improved strength even over conventional alloy strengthening mechanisms. (**a**) Cumulative distribution functions (CDFs) of each pop-in data set. A thermal activation model is also fit to each distribution and plotted here using solid lines. (**b**) A bar plot of average pop-in load for each data set. The dashed line represents strengthening that might be expected from a Cottrell atmosphere using the Labusch model, and the shaded region shows the theoretical strength of nickel.

of values of k and α and a concentration of 0.25 at.% Al, which is the equilibrium amount for the $L1_2$ phase, a total strength increase ranging from 74 MPa to 113 MPa is estimated. The dashed line in Fig. 7b shows the normalized estimated strengthening upper bound in comparison to the pre- and post-DP-HT samples. We see that this analysis dramatically underestimates the measured strength increase, indicating that the presence of Al solutes near the dislocation core alone is not sufficient to reconcile our results.

Next, we consider more traditional strengthening mechanisms associated with the presence of ordered domains in a matrix and compare to our pop-in results. We evaluate strengthening expected from shearing of ordered particles in a solid solution matrix, which includes effects of particle incoherency ($\Delta\sigma_C$), modulus mismatch between the precipitate and matrix ($\Delta\sigma_M$), and the formation of antiphase boundaries (APBs) as dislocations shear the ordered precipitate ($\Delta\sigma_O$). The first two phenomena are dominant just before the dislocation is able to shear and move through the precipitate, and the latter is relevant to the actual glide process through the ordered phase. The larger value of ($\Delta\sigma_C + \Delta\sigma_M$) or $\Delta\sigma_O$ is expected to be the total strength contribution from a precipitate shearing mechanism [60]. Each of these contributions can be determined using the following equations:

$$\Delta\sigma_C = M \cdot \alpha_\epsilon \cdot (G\epsilon_c)^{3/2} \cdot \left(\frac{rf}{0.5Gb}\right)^{1/2} \tag{4}$$

$$\Delta\sigma_M = M \cdot 0.0055(\Delta G)^{3/2} \cdot \left(\frac{2f}{G}\right)^{1/2} \cdot \left(\frac{r}{b}\right)^{\frac{3m}{2}-1} \tag{5}$$

$$\Delta\sigma_O = M \cdot 0.81 \cdot \frac{\gamma_{APB}}{2b} \cdot \left(\frac{3\pi f}{8}\right)^{1/2} \tag{6}$$

where M, the Taylor factor, is 3.06 for FCC structures [61], α_ϵ is a constant equal to 2.6 [62], G is the shear modulus of the matrix, ϵ_c is the constrained lattice misfit, r is the average size of precipitates, f is the volume fraction, b is the Burgers vector, ΔG is the difference in shear modulus between matrix and precipitate, m is a constant of value 0.85 [63], and γ_{APB} is the APB energy of the precipitate phase. Using materials constants for FCC Ni and $L1_2$ Ni_3Al [64], we find that the effect of shearing and APB formation is at least double that of coherency strengthening and modulus mismatch, so we focus only on the APB contribution. The APB energy of the $L1_2$ phase can be evaluated using a variety of computational methods and via TEM measurements of the stacking fault width, but values vary widely depending on imaging conditions and assumptions made during modeling. Therefore, we consider a range of γ_{APB} from 0.150 J/m^2 and 0.200 J/m^2, with most studies finding values around 0.170 – 0.190 J/m^2. Using these values for γ_{APB}, b = 2.52 Å, and f = 0.1, a strength increase from particle shearing, $\Delta\sigma_O$, ranges from 253–338 MPa. This still dramatically underestimates the strength increase of 814 MPa we see in samples after the DP-HT, indicating a traditional shearing mechanism is insufficient to explain our results. For comparison, the volume fraction of $L1_2$ phase in our samples would need to be at least 56% to see a similar increase in strength of 800 MPa, which we know to be inconsistent with our TEM imaging.

Finally, because the dislocation density decreases slightly after DP-HT (from 3.9×10^{13} m^{-2} to 1.0×10^{13} m^{-2}), we must also consider how the pre-existing dislocation content may impact pop-in behavior. While an increase in mean pop-in load may be attributed to a decreasing dislocation density, this behavior would also be associated with a characteristic broadening of the distribution of pop-in loads reflecting the finite sampling of small populations of dislocations [52]. Our distributions, rather, shift without a concomitant and proportional broadening, as measured by the ratio of the standard deviation to the mean of each distribution, which is found to be 0.171 and 0.126 for the deformed pre-DP-HT and deformed post-DP-HT samples, respectively. Additionally, we note that the density remains on the order of 10^{13} in the microindented samples both before and after DP-HT, making strong changes in strengthening from dislocation density alone unlikely. We confirm this assertion by calculating the contribution from Taylor hardening, expressed as [65]:

$$\tau_c = \alpha\mu b\sqrt{\rho} \tag{7}$$

where $\alpha = \sqrt{2}/(8\pi(1-\nu))$, μ is the shear modulus, b is the Burgers vector magnitude, ρ is the dislocation density, and ν is Poisson's ratio. Using material constants for Ni [66], dislocation densities measured for each deformed sample, and taking a range of α = 0.5 – 1, the maximum difference in strength before and after DP-HT due only to dislocation content is estimated to be 147 MPa, which is far lower than the measured difference of 900 MPa. It is clear that neither Cottrell-like solute atmosphere strengthening nor Taylor hardening are sufficient to account for the 40% increase in strength observed in this work. We hypothesize that the chemical ordering arising from the solute enrichment and the dislocation strain fields evident in the SAEDPs contribute substantially to strengthening. This motivates a more detailed analysis of the microstructure and dislocation state following the DP-HT.

3.3. Characterization of nanoscale ordered domains

We next explore the nature of the dislocation-templated ordering that leads to such large strengthening in this Ni–Al system, especially as there is no evidence of bulk-scale precipitation of an $L1_2$ phase (sufficient volume fractions or coherent scattering sizes to contribute to scattered X-ray intensities). One notable feature of both the microindented and rolled samples after DP-HT is the presence of paired

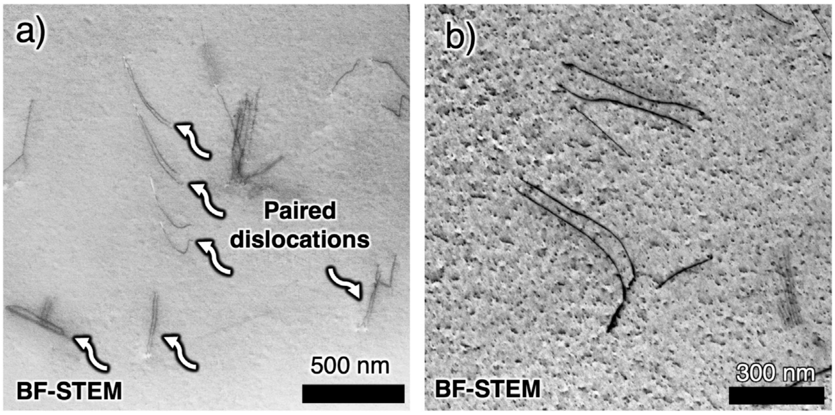

Fig. 8. Microscopic evaluation reveals presence of paired dislocations. (**a**) Bright field STEM (BF-STEM) micrograph of dislocation pairs distributed throughout a rolled, electropolished sample after DP-HT. (**b**) BF-STEM micrograph of paired dislocations in a microindented sample after DP-HT.

dislocations throughout the samples, as seen in Fig. 8a, b. Paired dislocations of this nature are frequently observed in $L1_2$-containing Ni-superalloy systems [67], and are attributed to the disruption of ordering and generation of an antiphase boundary (APB) by glide of matrix dislocations (which become super partial dislocations in the ordered precipitate). The coordinated motion of dislocation couples minimizes the energy penalty of the APB since the trailing dislocation restores the preferred stacking by annihilating the APB [68]. The presence of paired dislocations throughout our samples point to an ordered, more energetically complex field that dislocations must glide through compared to what would normally be expected for a simple solid solution.

Detailed electron microscopy is used to characterize the size, distribution, and spatial arrangement of the emergent ordered domains. Weak beam dark field (WB-DF) imaging using the (g, 3 g) condition along the [220] direction shows the precise location of several dislocations in a cold-rolled, post-DP-HT sample (Fig. 9a), and, in this same sample area, DF imaging using the (100) superlattice reflection reveals $L1_2$ ordered domains surrounding the dislocated region (Fig. 9b). Similar ordered domain formation was observed around at least five other investigated dislocations in both rolled and microindented samples and additional analysis was performed to rule out FIB-induced damage as the source of these domains (supplementary text). We quantify the spatial arrangement of the ordered domains using a cluster analysis to determine nearest neighbor distances (coloring in Fig. 9b), revealing that many of the most densely populated regions (dark blue domains) overlap directly with image intensity originating from the dislocation strain field, with regions further from the dislocations (top right and bottom left corners) displaying larger distances between neighbors. The sizes of the ordered domains are on the order of a few nanometers (2.7 nm ± 0.59 nm), (Fig. 9c) with equivalent size distributions showing a range of ordered domain diameters between approximately 1 and 5 nm (Fig. 9d). These sizes are small but consistent with predicted dislocation phase sizes and the dislocation strain field [13], and they represent length scales associated with clearly developed ordering beyond chemical short range order [69,70].

We infer from the lack of evidence for nanodomain formation in the undeformed, dislocation-free samples (Fig. 5) that nanodomains form only when a combination of dislocations and specific thermal conditions (DP-HT) are present. We also rule out the potential that dislocations formed after the $L1_2$ domains due to lattice misfit since the expected misfit between FCC Ni and $L1_2$ Ni_3Al is very low (0.3%), and there is no evidence of bulk $L1_2$ formation or dislocations in undeformed regions. Closer examination of these nanodomains near a dislocation through atomic-resolution STEM shows clear evidence of chemical ordering, outlined in orange in the atomic-resolution STEM image acquired along the [001] zone axis (Fig. 10a). These domains closely match regions with extensive contrast variations in Fourier-filtered images using the superlattice intensities (Fig. 10b). Along this [001] zone axis, $L1_2$ ordering exhibits a characteristic intensity modulation along alternating rows, where one row ("A") contains alternating Ni and Al atoms and the other ("B") contains only Ni as shown in the inset of Fig. 10a. A ratio (A/B) of the average intensity profiles along four different A and B type rows (acquired within the orange brackets in Fig. 10a) confirms the atomic scale modulation consistent with $L1_2$ ordering at nm length scale (Fig. 10c). Significantly, superlattice reflections are only present in FFTs acquired from within these ordered nanodomains, as evidenced through intensity profiles of FFTs along the (200) type g-vector from a region with ordering (orange in Fig. 10d) and without (black dashed lines), consistent with the selected-area electron diffraction (Figs. 3b and 4b).

3.4. Mechanisms governing dislocation defect phase formation

The phenomena observed here, namely nanoscale ordering emerging in dislocated regions, offers intriguing parallels to relevant alloy systems and phase evolution mechanisms, but with several key differences. While the presence of nanoscale ordering and chemical short range order has been a significant topic of discussion in Ni- and Co-containing medium entropy alloys, the formation of ordering in these systems is typically attributed to the presence of many types of solute atoms, with potentially competing interaction parameters, and generally near-equiatomic proportions [69,71]. The phenomena observed here differ quite drastically, as the presence of ordered domains manifests with a relatively small concentration of a single alloying element as long as dislocations and the DP-HT are supplied. Other anomalous behaviors have been reported for semi-dilute Ni–Al alloys, specifically in relation to resistivity measurements, known as the "k-effect", where resistivity increases suddenly upon aging [72]. While there is no established link to changes in strength, such changes in resistivity have been linked to SRO in binary Ni–Al and reveal hints of a more complex phase evolution present in this system. To develop an understanding of the formation mechanism for these nanodomains and to facilitate new design pathways that maximize material strength, we next examine hypotheses for the sequence of events leading to defect phase formation.

Turlo and Rupert previously examined dislocation phase formation in detail using hybrid Monte Carlo/ molecular dynamics simulations in several different FCC alloys, including Ni–Al [16]. They found that the $L1_2$ phase forms preferentially at dislocations when the heat treatment is performed in the two-phase field, consistent with heterogeneous nucleation. However, when the heat treatment is performed near the solvus line within the single-phase FCC field, $L1_2$ regions form which are stabilized by the stress field of the dislocations and would not

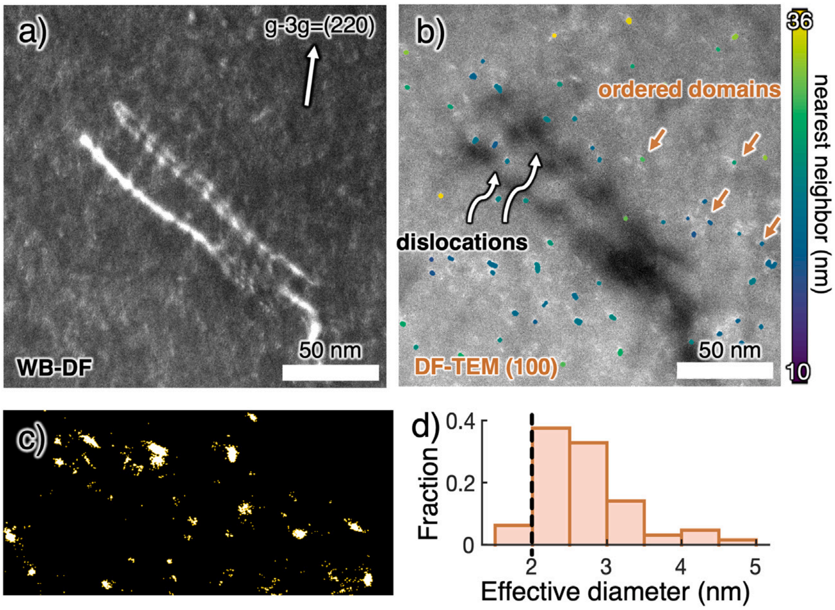

Fig. 9. Transmission electron microscopy confirms presence of nanoscale $L1_2$ ordered domains near heavily dislocated regions. (**a**) Weak beam dark field (WB-DF) micrograph of several dislocations in a rolled, electropolished sample after DP-HT, taken using the g-3g=(220) condition. (**b**) Dark field TEM (DF-TEM) micrograph taken using the (100) superlattice reflection with ordered domains colored according to nearest neighbor distance. (**c**) An example image of a mask used during detection and segmentation of ordered domains showing intensity under dark field imaging conditions. (**d**) Histogram showing the effective diameter of ordered domains. The black dashed line indicates the spatial resolution of the TEM under dark field imaging conditions. (For interpretation of the references to color in this figure legend, the reader is referred to the web version of this article.)

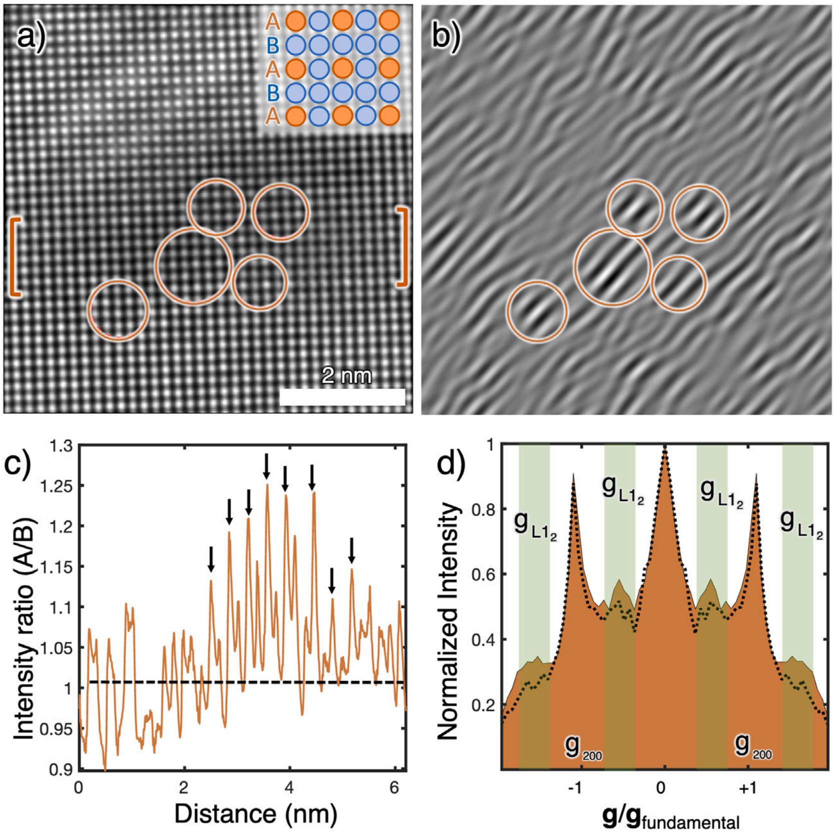

Fig. 10. Further microscopic evaluation confirms presence of nanoscale $L1_2$ ordered domains near heavily dislocated regions. (**a**) Atomic resolution STEM micrograph showing atomic column modulation in nano-scale ordered regions (orange circles determined from the Inverse Fast Fourier Transform along the superlattice reflections in (b)). The inset shows the alternating A and B rows of an $L1_2$ phase along the [001] zone axis. (**b**) A complementary inverse fast Fourier transform image of the region in (a), where the mask was placed around the superlattice features in reciprocal-space. Heavy distortions in the image directly correlate to ordered domains in real-space. (**c**) A plot of the ratio of intensities along A and B rows with black arrows indicating where A intensity is much higher than that of B on alternating atomic columns, indicating the presence of an ordered $L1_2$ phase. (**d**) Intensity plots taken along the (200) type g-vector on fast Fourier transforms (FFTs) acquired from both ordered (orange) and non-ordered (black dotted line) regions of the atomic-resolution STEM image.

be predicted by the bulk phase diagram. They take on a distinctive size and arrangement along the dislocation line in order to minimize the system energy, wherein they maintain a particle diameter of a few nanometers and a periodic arrangement along the dislocation line, again distinguishing these dislocation phases from bulk nucleation.

Based on our collective TEM imaging and diffraction evidence, we propose a mechanism whereby Al atoms, once attracted to a dislocation by its strain field, can more rapidly diffuse along the dislocation and establish the necessary conditions to drive a disorder-to-order transition. While chemical mapping via STEM-EDS cannot resolve chemical segregation in this system, we expect the super-saturated nature of this sample at room temperature and the favorable accommodation of larger Al atoms at dislocations to encourage solute segregation to dislocated regions. We estimate this propensity for segregation assuming a primary driving force based on elastic interactions in the highly strained region surrounding a dislocation. Accordingly, the enthalpy of segregation for Al in Ni can be estimated using the McLean model [73], expressed as:

$$\Delta H_{el}^{seg} = -\frac{2K_B\mu_A(V_B - V_A)^2}{3K_BV_A + 4\mu_AV_B} \tag{8}$$

where K is the bulk modulus, μ is the shear modulus, V is the molar volume, and A and B represent the solute and solvent, respectively. Using materials constants from the Materials Project [64,74], we calculate this to be $\Delta H_{el}^{seg} = 16.3$ kJ/mol for Ni–Al. In comparison to other dislocation phase-forming systems where chemical segregation to dislocations has been measured via APT, namely Fe–Mn ($\Delta H_{el}^{seg} = 0.83$ kJ/mol) and Pt–Au ($\Delta H_{el}^{seg} = 4.92$ kJ/mol), we see that segregation to dislocations is even more likely in our Ni–Al system. The time and temperature of the DP-HT is ensured to be long enough to allow this diffusion of Al to dislocations (supplementary text), and the sample is rapidly quenched, preventing phase evolution during cooling as evidenced by the lack of bulk $L1_2$ formation in undeformed regions of the sample. Once at the dislocation, Al can then rapidly diffuse via pipe diffusion, which is thought to be caused by solute-vacancy interactions within the core [75]. First principles calculations have found diffusion of Al in Ni to be two orders of magnitude higher at dislocation cores in comparison to the bulk [76], and phase field modeling has been used to evaluate the effect of this difference on solute atom behavior at dislocations [77]. The results reveal the formation of a modulation in chemical concentration of solute atoms and incomplete solute decoration along the dislocation line [77], which is consistent with our observations of globular ordered nanodomains and is similar to experimental observations in the Fe-Mn system [13,14]. Finally, this decoration of ordered domains in the vicinity of dislocations or in the wake of glissile dislocations (given the evolution in dislocation density) effectively hinders subsequent dislocation motion under loading, providing the strengthening effect we observe here.

Another potential formation pathway would involve the presence of excess vacancies introduced through quenching and deformation in our processing steps, thereby accelerating the kinetics of precipitation [78–80]. We estimate the excess vacancy concentrations expected after physical deformation as:

$$c_v^{XS} = \frac{\chi\sigma\Omega\epsilon}{Q_f} \tag{9}$$

where c_v^{XS} is the excess vacancy concentration, χ is a constant of order 0.1, σ is the yield stress, Ω is atomic volume, ϵ is strain, and Q_f is vacancy formation energy [81]. Excess vacancies formed from deformation are calculated as $8.9\ x\ 10^{-5}$ vacancy/Ni for microindented samples and $6.5\ x\ 10^{-4}$ vacancy/Ni for rolled samples. The amount of vacancies introduced by quenching is based on the difference between the equilibrium amount of vacancies at the higher temperature in comparison to room temperature. To estimate this, we use

$$c_v^{XS} = exp\left(\frac{-Q_f}{kT}\right)(1 - ZC_s) \tag{10}$$

where k is Boltzmann's constant, T is heat treatment temperature, and $(1 - ZC_s)$ is a correction term for an alloy system based on the coordination number, Z, and solute concentration, c_s [82]. Normalized vacancy concentrations are found to be $1.2\ x\ 10^{-6}$ vacancy/Ni for the first heat treatment and $2.6\ x\ 10^{-7}$ vacancy/Ni for the DP-HT, much greater than the equilibrium vacancy concentration in Ni at room temperature of $8.2\ x\ 10^{-25}$ vacancy/Ni [83]. Because excess vacancies are introduced in each processing step, we might expect ordered domains to form at any point along the processing route if vacancies alone are sufficient to encourage phase evolution via nucleation; however, two factors rule out a supersaturation of vacancies as mediating the formation of defect phases. First, the absence of chemical ordering following the deformation step (and prior to DP-HT) suggests that plastic deformation alone is not sufficient to drive the nanoscale phase transition. Second, dislocation-free regions following DP-HT, where quenched-in excess vacancies would be present, do not show superlattice reflections in the electron diffraction patterns. This collective evidence points to the importance of relatively long-range strain fields ($\sim r^{-1}$) from a network of dislocations and a secondary segregation heat treatment that promotes chemical enrichment and ultimately ordering.

4. Conclusions

We have experimentally demonstrated, using a model binary Ni–Al alloy, that the introduction of dislocations and a subsequent defect-targeted heat treatment can promote localized defect phases not predicted by the bulk phase diagram, yet which are more potent than conventional strengthening mechanisms. Specifically, an FCC Ni–Al alloy with pre-existing dislocations exhibits the formation of nanoscale, $L1_2$ ordered domains which do not form in the absence of dislocations. As an expansion on previous dislocation phase studies where chemical segregation to dislocations is clear [13,14], we also directly show evidence for chemical ordering as well as increased dislocation pinning and strengthening from domains that form exactly at the strengthening features (dislocations). Measurements of the local nanomechanical response demonstrate that the shear strength is found to increase by 40% after the DP-HT and the formation of the ordered motifs, approaching the order of magnitude of the theoretical strength. The impact of dislocations on the disorder to order phase transformation seen in this work points to new ways in which simple processing steps (cold rolling, segregation annealing) can be used to engineer "defects by design;" indeed, we anticipate that our strategy is applicable to a broad canvas of materials capable of hosting dislocations. Our work firmly establishes the defect phase paradigm and demonstrates its potential for achieving attractive property gains, as well as new pathways in defect and alloy design that enable the development of novel engineered microstructures.

CRediT authorship contribution statement

H.C. Howard: Writing – review & editing, Writing – original draft, Visualization, Methodology, Investigation, Formal analysis, Data curation. **W.S. Cunningham:** Writing – review & editing, Writing – original draft, Visualization, Methodology, Investigation, Formal analysis, Data curation. **A. Genc:** Writing – review & editing, Investigation. **B.E. Rhodes:** Writing – review & editing, Methodology, Investigation, Formal analysis. **B. Merle:** Writing – review & editing, Methodology, Investigation, Formal analysis, Data curation. **T.J. Rupert:** Writing – review & editing, Project administration, Methodology, Funding acquisition, Conceptualization. **D.S. Gianola:** Writing – review & editing, Writing – original draft, Visualization, Project administration, Methodology, Funding acquisition, Formal analysis, Conceptualization.

Declaration of competing interest

The authors declare that they have no known competing financial interests or personal relationships that could have appeared to influence the work reported in this paper.

Acknowledgments

We would like to acknowledge Anton Van der Ven, Christoph Gammer, and G. Robert Odette for constructive discussions about this research. This research was sponsored by the Army Research Office, United States under Grant Number W911NF-21-1–0288 . The views and conclusions contained in this document are those of the authors and should not be interpreted as representing the official policies, either expressed or implied, of the Army Research Office or the U.S. Government. The U.S. Government is authorized to reproduce and distribute reprints for Government purposes notwithstanding any copyright notation herein. This work employed the MRL Shared Experimental Facilities, which are supported by the MRSEC Program of the NSF under Award No. DMR 2308708; a member of the NSF-funded Materials Research Facilities Network. Acquisition of the Spectra STEM used for the studies was supported in part by the Army Research Office, United States under Grant No. 294 W911NF-20–1–0326. W. S. C. acknowledges support from the National Science Foundation MPS-Ascend Postdoctoral Research Fellowship under Grant No. 2316692. This material is also based upon work supported by the National Science Foundation Graduate Research Fellowship under Grant No. 2139319. Any opinion, findings, and conclusions or recommendations expressed in this material are those of the authors(s) and do not necessarily reflect the views of the National Science Foundation. B.M.'s contribution to this project has received funding from the European Research Council (ERC) under the European Union's Horizon 2020 research and innovation programme (grant agreement No 949626). B.M. furthermore acknowledges financial support by BaCaTec at Friedrich-Alexander-Universität Erlangen-Nürnberg (FAU). B. E. R. gratefully acknowledges support by the U.S. Department of Defense (DoD) through the National Defense Science & Engineering Graduate (NDSEG) Fellowship Program.

Appendix A. Supplementary data

Supplementary material related to this article can be found online at https://doi.org/10.1016/j.actamat.2025.120887.

References

[1] D. Blavette, E. Cadel, C. Pareige, B. Deconihout, P. Caron, Phase transformation and segregation to lattice defects in Ni-base superalloys, Microsc. Microanal. 13 (6) (2007) 464–483.

[2] T. Watanabe, Grain boundary engineering: historical perspective and future prospects, J. Mater. Sci. 46 (12) (2011) 4095–4115.

[3] M. Zhao, W. Pan, C. Wan, Z. Qu, Z. Li, J. Yang, Defect engineering in development of low thermal conductivity materials: A review, J. Eur. Ceram. Soc. (ISSN: 0955-2219) 37 (1) (2017) 1–13.

[4] S. Korte-Kerzel, T. Hickel, L. Huber, D. Raabe, S. Sandlöbes-Haut, M. Todorova, J. Neugebauer, Defect phases–thermodynamics and impact on material properties, Int. Mater. Rev. 67 (1) (2022) 89–117.

[5] D. Raabe, S. Sandlöbes, J. Millán, D. Ponge, H. Assadi, M. Herbig, P.-P. Choi, Segregation engineering enables nanoscale martensite to austenite phase transformation at grain boundaries: a pathway to ductile martensite, Acta Mater. 61 (16) (2013) 6132–6152.

[6] T. Frolov, D.L. Olmsted, M. Asta, Y. Mishin, Structural phase transformations in metallic grain boundaries, Nat. Commun. 4 (1) (2013) 1899.

[7] P.R. Cantwell, T. Frolov, T.J. Rupert, A.R. Krause, C.J. Marvel, G.S. Rohrer, J.M. Rickman, M.P. Harmer, Grain boundary complexion transitions, Annu. Rev. Mater. Res. 50 (2020) 465–492.

[8] M.S. Titus, R.K. Rhein, P.B. Wells, P.C. Dodge, G.B. Viswanathan, M.J. Mills, A. Van der Ven, T.M. Pollock, Solute segregation and deviation from bulk thermodynamics at nanoscale crystalline defects, Sci. Adv. 2 (12) (2016) e1601796.

[9] J. Miao, C.E. Slone, T.M. Smith, C. Niu, H. Bei, M. Ghazisaeidi, G.M. Pharr, M.J. Mills, The evolution of the deformation substructure in a Ni-Co-Cr equiatomic solid solution alloy, Acta Mater. 132 (2017) 35–48.

[10] T.M. Smith, B.D. Esser, B. Good, M.S. Hooshmand, G.B. Viswanathan, C.M.F. Rae, M. Ghazisaeidi, D.W. McComb, M.J. Mills, Segregation and phase transformations along superlattice intrinsic stacking faults in Ni-based superalloys, Met. Mater. Trans. A 49 (2018) 4186–4198.

[11] S.Y. Hu, L.Q. Chen, Solute segregation and coherent nucleation and growth near a dislocation—a phase-field model integrating defect and phase microstructures, Acta Mater. 49 (3) (2001) 463–472.

[12] X. Zhou, J.R. Mianroodi, A. Kwiatkowski da Silva, T. Koenig, G.B. Thompson, P. Shanthraj, D. Ponge, B. Gault, B. Svendsen, D. Raabe, The hidden structure dependence of the chemical life of dislocations, Sci. Adv. 7 (16) (2021) eabf0563.

[13] M. Kuzmina, M. Herbig, D. Ponge, S. Sandlöbes, D. Raabe, Linear complexions: Confined chemical and structural states at dislocations, Science 349 (6252) (2015) 1080–1083.

[14] A. Kwiatkowski Da Silva, G. Leyson, M. Kuzmina, D. Ponge, M. Herbig, S. Sandlöbes, B. Gault, J. Neugebauer, D. Raabe, Confined chemical and structural states at dislocations in Fe-9wt% Mn steels: A correlative TEM-atom probe study combined with multiscale modelling, Acta Mater. 124 (2017) 305–315.

[15] V. Turlo, T.J. Rupert, Dislocation-assisted linear complexion formation driven by segregation, Scr. Mater. 154 (2018) 25–29.

[16] V. Turlo, T.J. Rupert, Prediction of a wide variety of linear complexions in face centered cubic alloys, Acta Mater. 185 (2020) 129–141.

[17] T. Frolov, Y. Mishin, Phases, phase equilibria, and phase rules in low-dimensional systems, J. Chem. Phys. 143 (4) (2015).

[18] C.G. Van de Walle, J. Neugebauer, First-principles surface phase diagram for hydrogen on GaN surfaces, Phys. Rev. Lett. 88 (6) (2002) 066103.

[19] Y.L. Li, L.Q. Chen, Temperature-strain phase diagram for $BaTiO_3$ thin films, Appl. Phys. Lett. 88 (7) (2006).

[20] X. Shi, J. Luo, Developing grain boundary diagrams as a materials science tool: a case study of nickel-doped molybdenum, Phys. Rev. B— Condens. Matter Mater. Phys. 84 (1) (2011) 014105.

[21] T.P. Matson, C.A. Schuh, Phase and defect diagrams based on spectral grain boundary segregation: A regular solution approach, Acta Mater. 265 (2024) 119584.

[22] G.P.M. Leyson, B. Grabowski, J. Neugebauer, Multiscale description of dislocation induced nano-hydrides, Acta Mater. 89 (2015) 50–59.

[23] D. Singh, V. Turlo, D.S. Gianola, T.J. Rupert, Linear complexions directly modify dislocation motion in face-centered cubic alloys, Mater. Sci. Eng.: A 870 (2023) 144875.

[24] D. Singh, D.S. Gianola, T.J. Rupert, Dislocation breakaway from nanoparticle array linear complexions: Plasticity mechanisms and strength scaling laws, Materialia 32 (2023) 101929.

[25] S.E. Prameela, T.M. Pollock, D. Raabe, M.A. Meyers, A. Aitkaliyeva, K.-L. Chintersingh, Z.C. Cordero, L. Graham-Brady, Materials for extreme environments, Nat. Rev. Mater. 8 (2) (2023) 81–88.

[26] A.A. Coelho, TOPAS and TOPAS-Academic: an optimization program integrating computer algebra and crystallographic objects written in C++, J. Appl. Crystallogr. 51 (1) (2018) 210–218.

[27] W.C. Oliver, G.M. Pharr, An improved technique for determining hardness and elastic modulus using load and displacement sensing indentation experiments, J. Mater. Res. 7 (6) (1992) 1564–1583.

[28] P. Feldner, B. Merle, M. Göken, Determination of the strain-rate sensitivity of ultrafine-grained materials by spherical nanoindentation, J. Mater. Res. 32 (8) (2017) 1466–1473.

[29] J. Schindelin, I. Arganda-Carreras, E. Frise, V. Kaynig, M. Longair, T. Pietzsch, S. Preibisch, C. Rueden, S. Saalfeld, B. Schmid, et al., Fiji: an open-source platform for biological-image analysis, Nature Methods 9 (7) (2012) 676–682.

[30] R. Haase, L.A. Royer, P. Steinbach, D. Schmidt, A. Dibrov, U. Schmidt, M. Weigert, N. Maghelli, P. Tomancak, F. Jug, et al., CLIJ: GPU-accelerated image processing for everyone, Nature Methods 17 (1) (2020) 5–6.

[31] L. Ma, L. Levine, R. Dixson, D. Smith, D. Bahr, Effect of the spherical indenter tip assumption on the initial plastic yield stress, Nanoindentation Mater. Sci. (2012) 25–52.

[32] Y.J. Park, G.M. Pharr, Nanoindentation with spherical indenters: finite element studies of deformation in the elastic–plastic transition regime, Thin Solid Films 447 (2004) 246–250.

[33] D. Tabor, The Hardness of Metals, Oxford University Press, 2000.

[34] F.G. Coury, C. Miller, R. Field, M. Kaufman, On the origin of diffuse intensities in fcc electron diffraction patterns, Nature 622 (7984) (2023) 742–747.

[35] F. Walsh, M. Zhang, R.O. Ritchie, A.M. Minor, M. Asta, Extra electron reflections in concentrated alloys do not necessitate short-range order, Nat. Mater. 22 (8) (2023) 926–929.

[36] S.A. Syed Asif, J.B. Pethica, Nanoindentation creep of single-crystal tungsten and gallium arsenide, Phil. Mag. A 76 (6) (1997) 1105–1118.

[37] T.F. Page, W.C. Oliver, C.J. McHargue, The deformation behavior of ceramic crystals subjected to very low load (nano) indentations, J. Mater. Res. 7 (2) (1992) 450–473.

[38] M.A. Lodes, A. Hartmaier, M. Göken, K. Durst, Influence of dislocation density on the pop-in behavior and indentation size effect in CaF_2 single crystals: Experiments and molecular dynamics simulations, Acta Mater. 59 (11) (2011) 4264–4273.

[39] J.G. Swadener, E.P. George, G.M. Pharr, The correlation of the indentation size effect measured with indenters of various shapes, J. Mech. Phys. Solids 50 (4) (2002) 681–694.

[40] J.R. Morris, H. Bei, G.M. Pharr, E.P. George, Size effects and stochastic behavior of nanoindentation pop in, Phys. Rev. Lett. 106 (16) (2011) 165502.

[41] J. Li, K.J. Van Vliet, T. Zhu, S. Yip, S. Suresh, Atomistic mechanisms governing elastic limit and incipient plasticity in crystals, Nature 418 (6895) (2002) 307–310.
[42] K.L. Johnson, Contact Mechanics, Cambridge University Press, 1987.
[43] S. Ogata, J. Li, N. Hirosaki, Y. Shibutani, S. Yip, Ideal shear strain of metals and ceramics, Phys. Rev. B 70 (10) (2004) 104104.
[44] C.A. Schuh, A.C. Lund, Application of nucleation theory to the rate dependence of incipient plasticity during nanoindentation, J. Mater. Res. 19 (7) (2004) 2152–2158.
[45] J.K. Mason, A.C. Lund, C.A. Schuh, Determining the activation energy and volume for the onset of plasticity during nanoindentation, Phys. Rev. B 73 (5) (2006) 054102.
[46] F. Seitz, On the formation of dislocations from vacancies, Phys. Rev. 79 (5) (1950) 890.
[47] H. Bei, Y.Z. Xia, R.I. Barabash, Y.F. Gao, A tale of two mechanisms: Strain-softening versus strain-hardening in single crystals under small stressed volumes, Scr. Mater. 110 (2016) 48–52.
[48] M.D. Uchic, D.M. Dimiduk, J.N. Florando, W.D. Nix, Sample dimensions influence strength and crystal plasticity, Science 305 (5686) (2004) 986–989.
[49] W.D. Nix, J.R. Greer, G. Feng, E.T. Lilleodden, Deformation at the nanometer and micrometer length scales: Effects of strain gradients and dislocation starvation, Thin Solid Films 515 (6) (2007) 3152–3157.
[50] J.R. Greer, J.T.M. De Hosson, Plasticity in small-sized metallic systems: Intrinsic versus extrinsic size effect, Prog. Mater. Sci. 56 (6) (2011) 654–724.
[51] T.L. Li, H. Bei, J.R. Morris, E.P. George, Y. Gao, Scale effects in convoluted thermal/spatial statistics of plasticity initiation in small stressed volumes during nanoindentation, Mater. Sci. Technol. 28 (9–10) (2012) 1055–1059.
[52] Y. Gao, H. Bei, Strength statistics of single crystals and metallic glasses under small stressed volumes, Prog. Mater. Sci. 82 (2016) 118–150.
[53] H. Pottebohm, G. Neite, E. Nembach, Elastic properties (the stiffness constants, the shear modulus and the dislocation line energy and tension) of Ni-Al solid solutions and of the Nimonic alloy PE16, Mater. Sci. Eng. 60 (3) (1983) 189–194.
[54] R. Labusch, A statistical theory of solid solution hardening, Phys. Status Solidi (B) 41 (2) (1970) 659–669.
[55] G.P.M. Leyson, W.A. Curtin, Friedel vs. Labusch: the strong/weak pinning transition in solute strengthened metals, Phil. Mag. 93 (19) (2013) 2428–2444.
[56] L.A. Gypen, A. Deruyttere, Multi-component solid solution hardening: Part 1: Proposed model, J. Mater. Sci. 12 (1977) 1028–1033.
[57] Y. Mishima, S. Ochiai, N. Hamao, M. Yodogawa, T. Suzuki, Solid solution hardening of nickel—role of transition metal and B-subgroup solutes—, Trans. Japan Inst. Met. 27 (9) (1986) 656–664.
[58] M.-X. Wang, H. Zhu, G.-J. Yang, K. Liu, J.-F. Li, L.-T. Kong, Solid-solution strengthening effects in binary Ni-based alloys evaluated by high-throughput calculations, Mater. Des. 198 (2021) 109359.
[59] R.L. Fleischer, Substitutional solution hardening, Acta Metall. 11 (3) (1963) 203–209.
[60] Q. Wang, Z. Li, S. Pang, X. Li, C. Dong, P.K. Liaw, Coherent precipitation and strengthening in compositionally complex alloys: a review, Entropy 20 (11) (2018) 878.
[61] W.F. Hosford, Mechanical Behavior of Materials, Cambridge University Press, 2010.
[62] V. Gerold, H. Haberkorn, On the critical resolved shear stress of solid solutions containing coherent precipitates, Phys. Status Solidi (B) 16 (2) (1966) 675–684.
[63] E. Nembach, Precipitation hardening caused by a difference in shear modulus between particle and matrix, Phys. Status Solidi (A) 78 (2) (1983) 571–581.
[64] A. Jain, S.P. Ong, G. Hautier, W. Chen, W.D. Richards, S. Dacek, S. Cholia, D. Gunter, D. Skinner, G. Ceder, et al., Commentary: The Materials Project: A materials genome approach to accelerating materials innovation, APL Mater. 1 (1) (2013).
[65] W. Cai, W.D. Nix, Imperfections in Crystalline Solids, Cambridge University Press, 2016.
[66] E.A. Brandes, G.B. Brook, Smithells Metals Reference Book, Elsevier, 2013.
[67] W. Hüther, B. Reppich, Interaction of dislocations with coherent, stress-free, ordered particles, Int. J. Mater. Res. 69 (10) (1978) 628–634.
[68] H.V. Gleiter, E. Hornbogen, Precipitation hardening by coherent particles, Mater. Sci. Eng. 2 (6) (1968) 285–302.
[69] R. Zhang, S. Zhao, J. Ding, Y. Chong, T. Jia, C. Ophus, M. Asta, R.O. Ritchie, A.M. Minor, Short-range order and its impact on the CrCoNi medium-entropy alloy, Nature 581 (7808) (2020) 283–287.
[70] Q.-J. Li, H. Sheng, E. Ma, Strengthening in multi-principal element alloys with local-chemical-order roughened dislocation pathways, Nat. Commun. 10 (1) (2019) 3563.
[71] J. Ding, Q. Yu, M. Asta, R.O. Ritchie, Tunable stacking fault energies by tailoring local chemical order in CrCoNi medium-entropy alloys, Proc. Natl. Acad. Sci. 115 (36) (2018) 8919–8924.
[72] E.A. Starke Jr., V. Gerold, A.G. Guy, An investigation of the k-effect in Nickel-Aluminum alloys, Acta Metall. 13 (9) (1965) 957–964.
[73] D. McLean, Grain boundaries in metals, 1957.
[74] M. De Jong, W. Chen, T. Angsten, A. Jain, R. Notestine, A. Gamst, M. Sluiter, C. Krishna Ande, S. Van Der Zwaag, J.J. Plata, et al., Charting the complete elastic properties of inorganic crystalline compounds, Sci. Data 2 (1) (2015) 1–13.
[75] G.R. Love, Dislocation pipe diffusion, Acta Metall. 12 (6) (1964) 731–737.
[76] W. Luke, A First Principles Study of Pipe Diffusion in Nickel (Ph.D. thesis), Dissertation, Wrigth State University, 2020.
[77] A. Varma, P. Pant, M.P. Gururajan, Dislocation assisted phase separation: a phase field study, Acta Mater. 244 (2023) 118529.
[78] W. Sun, Y. Zhu, R. Marceau, L. Wang, Q. Zhang, X. Gao, C. Hutchinson, Precipitation strengthening of aluminum alloys by room-temperature cyclic plasticity, Science 363 (6430) (2019) 972–975.
[79] X.L. Ma, S.E. Prameela, P. Yi, M. Fernandez, N.M. Krywopusk, L.J. Kecskes, T. Sano, M.L. Falk, T.P. Weihs, Dynamic precipitation and recrystallization in Mg-9wt.% Al during equal-channel angular extrusion: A comparative study to conventional aging, Acta Mater. 172 (2019) 185–199.
[80] S.E. Prameela, P. Yi, B. Medeiros, V. Liu, L.J. Kecskes, M.L. Falk, T.P. Weihs, Deformation assisted nucleation of continuous nanoprecipitates in Mg–Al alloys, Materialia 9 (2020) 100583.
[81] A. Deschamps, G. Fribourg, Y. Brechet, J.L. Chemin, C.R. Hutchinson, In situ evaluation of dynamic precipitation during plastic straining of an Al–Zn–Mg–Cu alloy, Acta Mater. 60 (5) (2012) 1905–1916.
[82] J.A. Wert, Vacancy concentrations in quenched binary alloys, Acta Metall. 28 (10) (1980) 1361–1373.
[83] A. Metsue, A. Oudriss, X. Feaugas, Hydrogen solubility and vacancy concentration in nickel single crystals at thermal equilibrium: New insights from statistical mechanics and ab initio calculations, J. Alloys Compd. 656 (2016) 555–567.